Quantum Inf Process (2016) 15:5315–5338
DOI 10.1007/s11128-015-1162-2

Integrated optics architecture for trapped-ion quantum information processing

D. Kielpinski[1] · C. Volin[2] · E. W. Streed[1,3] · F. Lenzini[1,4] · M. Lobino[1,4]

Received: 11 December 2014 / Accepted: 17 October 2015 / Published online: 23 November 2015

Abstract Standard schemes for trapped-ion quantum information processing (QIP) involve the manipulation of ions in a large array of interconnected trapping potentials. The basic set of QIP operations, including state initialization, universal quantum logic, and state detection, is routinely executed within a single array site by means of optical operations, including various laser excitations as well as the collection of ion fluorescence. Transport of ions between array sites is also routinely carried out in microfabricated trap arrays. However, it is still not possible to perform optical operations in parallel across all array sites. The lack of this capability is one of the major obstacles to scalable trapped-ion QIP and presently limits exploitation of current microfabricated trap technology. Here we present an architecture for scalable integration of optical operations in trapped-ion QIP. We show theoretically that diffractive mirrors, monolithically fabricated on the trap array, can efficiently couple light between trap array sites and optical waveguide arrays. Integrated optical circuits constructed from these waveguides can be used for sequencing of laser excitation and fluorescence collection. Our scalable architecture supports all standard QIP operations, as well as photon-mediated entanglement channels, while offering substantial performance improvements over current techniques.

Keywords Trapped ions · Quantum information processing · Diffractive mirrors · Integrated optics · Optical waveguides

✉ D. Kielpinski
dave.kielpinski@gmail.com

1 Centre for Quantum Dynamics, Griffith University, Brisbane, QLD, Australia

2 Georgia Tech Research Institute, Atlanta, GA, USA

3 Institute for Glycomics, Griffith University, Southport, QLD, Australia

4 Queensland Micro- and Nanotechnology Centre, Griffith University, Brisbane, QLD, Australia

1 Introduction

1.1 Motivation and background

Quantum information processing (QIP) promises remarkable advances in computing and communications technology, and the implementation of large-scale QIP is now a major goal in atomic, optical, and solid-state physics. Among the potential implementations, trapped ions stand out as satisfying many key criteria. Trapped ions can store quantum information for many minutes, their quantum states can be accurately detected, and high-accuracy, deterministic quantum logic gates have been demonstrated, while they are readily interfaced with quantum states of light for communication applications [1]. However, as with all current QIP implementations, scalability to hundreds or thousands of qubits remains an outstanding task.

The Kielpinski-Monroe-Wineland (KMW) architecture [2] has become a widely accepted roadmap for large-scale trapped-ion QIP. In the KMW architecture, small numbers of ions are trapped at many sites in a large array of interconnected ion traps. Well-known techniques permit state initialization and detection, as well as a complete set of quantum logic gates [1]. In particular, multiqubit logic gates can be performed between ions in a single array site by exploiting the Coulomb coupling of the ion motion. Ions are physically interchanged, or "shuttled," to transport quantum information between array sites. The combination of shuttling with local multiqubit gates enables large computational operations that span the entire trap array. Since the original KMW proposal, ion shuttling operations have been demonstrated by many groups using microfabricated ion trap arrays. A recent proposal [3] extends the KMW architecture by using ion–photon interfacing, as well as physical ion interchange, to perform operations between array sites. The KMW architecture also appears favorable for implementing quantum repeaters for long-distance quantum communication [4].

To achieve scalability in the KMW architecture, it is essential to perform all the elementary operations in parallel at hundreds or thousands of sites in the trap array [5]. State measurement requires the delivery of resonant laser light and the collection of ion fluorescence at each site. Motional quantum logic gates also require the delivery of off-resonant laser light to each site, possibly from multiple directions at once. Ion–photon interfacing and quantum communication impose a further demand that ion fluorescence should be collected into a single coherent optical mode. All these operations must be performed synchronously, rapidly, and in parallel, posing a significant challenge for optical integration.

Integration of optics into the KMW architecture must achieve spatial and temporal control of excitation and fluorescence modes over a large number of array sites, while remaining compatible with the microfabricated ion trap arrays used for shuttling. First, ion fluorescence at each array site must be collected and spatially mode-matched to an external optical collection system. Conversely, the spatial mode of externally delivered excitation light must be focused appropriately into the array geometry. Second, externally delivered excitation light must be switched temporally, at least at the sub-microsecond timescale of logic gates. For optimized ion–photon networking and quantum communication applications, both excitation and collection light should be temporally switched on the timescale of a typical atomic decay time ($\sim$10 ns).

Theoretical studies have assessed and compared potential technologies for spatial mode-matching, both collection and focusing, in the KMW architecture [6,7]. Some of these technologies have been demonstrated in proof-of-principle experiments [8–13]. Among these technologies, diffractive optics appear very well suited to fluorescence collection [7]. Diffractive optics arrays are readily scalable through microfabrication, while individual optics maintain high collection efficiency [9] and excellent imaging qualities [14], implying efficient collection into a single optical mode.

Options for temporal switching have been discussed in the literature [6], but have received less attention so far. Microelectromechanical (MEMS) mirrors have been designed [15] and tested [16] with the aim of delivering a single laser beam to multiple trap array sites. Operations within a single array site have been demonstrated very recently [17] with a laser beam slew rate of 5 m/s. For a typical array site spacing of $\gtrsim 200\,\mu\mathrm{m}$, the time to switch the laser beam is therefore $\gtrsim 40\,\mu\mathrm{s}$, an order of magnitude longer than typical operation times. The laser beam must be switched off during this slew time, e.g., with an acousto-optic modulator, to avoid crosstalk between sites. This scheme therefore requires the lasers to be switched off the vast majority of the time. However, total laser power is likely to be a scarce resource for large-scale QIP. A complete assessment of the physical requirements for a trapped-ion quantum computer of 300 logical bits suggested that continuous delivery of 1980 laser beams, each of 10–200 mW power, would be necessary [5]. Accounting for MEMS slew times would reduce the duty cycle of laser operation by a factor of 10, so that the UV laser source is required to deliver >100 W or even kW of power. This task is beyond the current limits of UV laser technology.

Here we propose a scalable, robust, and tightly integrated architecture for trapped-ion QIP. The architecture is shown in Fig. 1 and consists of integrated diffractive mirrors interfaced with reconfigurable planar waveguide circuits (PLCs) to achieve focusing and collection spatial modes and 100 ps shaping of temporal modes. Diffractive mirrors with high numerical aperture are fabricated directly on the electrode structure of a microfabricated planar trap array. These mirrors define the spatial modes for collection of fluorescence and for delivery of excitation light at individual array sites. Excitation light is delivered through planar waveguide circuits (PLCs), which electro-optically switch the light between defined spatial modes on 100 ps timescales. Similarly, fluorescence light is collected into PLCs for multiplexing onto photodetectors (for ion state detection) or single-mode fibers (for quantum communication). The combination of these technologies enables parallel operations to be performed over high-density trap arrays: $\sim$50 sites/cm along each RF rail, or a spacing of $\sim 200\,\mu\mathrm{m}$ between array sites, with operation times and total laser powers that are comparable to current experiments.

2 On-chip diffractive mirrors

The on-chip diffractive mirrors define the spatial modes for the two key optical tasks: collection of fluorescence and delivery of excitation light. Conceptually, diffractive optics can be considered as diffraction gratings with a grating period that varies across the device. For instance, light rays striking a diffractive mirror at normal incidence

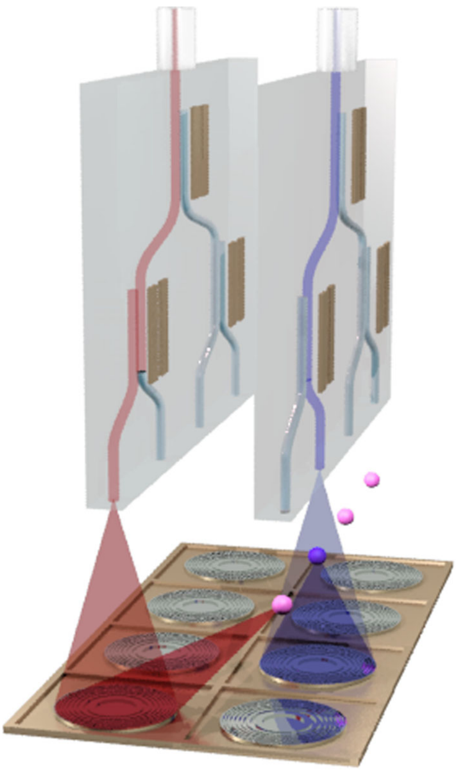

Fig. 1 Overview of integrated optics architecture. Planar waveguide circuits (PLCs; *gray blocks*, above) provide excitation light to, and collect fluorescence from, an array of ions (small spheres). Spatial mode-matching is achieved through diffractive mirrors (circular patterns) microfabricated directly onto a surface-electrode ion trap (*gold surface*). Electro-optic devices on the PLCs perform optical switching and frequency-shifting operations. In the depicted implementation, a linear array of ions is trapped at a spacing of $\gtrsim 200\,\mu$m. One layer of PLCs collects fluorescence (modes shown in blue) while another performs excitation of a selected ion (mode shown in red). A detailed implementation supporting full QIP is discussed below (see Sect. 4 and Fig. 7)

can be reflected and diffracted back toward the optic axis. If the diffraction angle is proportional to the distance from the device center, the device can be used to reflect and focus a collimated beam, or equivalently it can collimate a point source. The grating period, and its variation across the device, can be chosen nearly arbitrarily. Hence, optical aberration can often be eliminated in the design stage, even for optics with very high numerical aperture. Diffractive optics with numerical aperture up to 0.95 have been demonstrated to focus light without aberration [18].

Microfabricated surface-electrode ion traps are ideal for integration of diffractive mirrors. The electrodes present a nearly complete half-plane available for placement of the mirrors. Bare aluminum, a preferred metal for making electrodes, reflects over 90 % of light in the near-UV wavelengths of interest for Yb^+, Ca^+, and Ba^+. Unlike in-vacuum refractive optics and shaped mirrors, the topography of the diffractive mirror should not alter the electrical performance of the trap. The diffractive structure requires only $\sim$100 nm height variation of the electrode, much smaller than the ion-electrode distance, which is usually at least tens of μm.

The chief drawback of diffractive optics is that only some incident light is diffracted into the desired mode, as happens for any diffraction grating. The diffraction efficiency in first demonstrations of fluorescence collection was only 30 % [9], but simulations show that efficiency can be raised to 60 % for transmissive optics [19] and above 80 % for reflective optics [20] in reasonable fabrication scenarios.

2.1 Design of diffractive mirrors

The goal in designing a diffractive mirror is to transform a given input spatial mode into another given output spatial mode with the highest practical mode overlap and diffraction efficiency. The mirror design is usefully specified in terms of a spatial phase function and a grating design function. The spatial phase function $\Delta\phi(x, y)$ is equal to the optical phase imparted by the mirror at the position (x, y) and determines the local period of the diffraction grating,

$$\Lambda(x, y) = 2\pi \left|\nabla_{\mathrm{T}} \Delta\phi(x, y)\right|^{-1} \qquad \text{where} \tag{1}$$

$$\nabla_{\mathrm{T}} \equiv \hat{x}\frac{\partial}{\partial x} + \hat{y}\frac{\partial}{\partial y} \tag{2}$$

is the transverse gradient operator. The grating design function $H(d)$ specifies the height of the grating structure at a local position $0 < d < \Lambda$ within a single grating period Λ. Together, the spatial phase and grating design functions specify the lithographic masks that are used to actually fabricate the device. The design flow can be separated into several steps.

First, we determine the spatial phase function. To this end, we approximate the input and output modes as bundles of rays that pass through reference input and output surfaces. We approximate the mirror as an infinitely thin reflecting plate that imparts an optical path length $\Delta\ell(x, y) = \lambda\Delta\phi(x, y)/(2\pi)$, where λ is the wavelength of the light. By ray tracing from the input reference surface, by way of the mirror, to the output reference surface, we obtain the wave aberration for each ray at the output [21]. We choose a suitable cost function to summarize the wave aberration, for instance the root-mean-square aberration over all input rays. Numerically optimizing the optical path length to minimize the cost function then yields the spatial phase function $\Delta\phi(x, y)$.

Second, we determine a grating design function that provides high diffraction efficiency throughout the relevant range of grating periods. In principle, a fully optimized design would allow the grating design function to vary as a function of position (x, y). However, for reflective optics, good results can be obtained without this additional complication. It is enough to consider a single grating design function $H(d/\Lambda)$ that depends only on the local normalized position $d/\Lambda \in [0, 1]$. For the present application, fabrication constraints generally require us to use a piecewise constant grating design function, creating a so-called multilevel optic.

Figure 2 shows a suitable four-level design and a simulation of its diffraction efficiency, obtained from the electromagnetic simulation technique of rigorous coupled-wave analysis (RCWA; [22]). Since RCWA is only directly applicable to grating structures with a constant, uniform period, we first obtain designs that were optimized for particular grating periods using a genetic algorithm search. The final grating design function represents a compromise between these fixed-period designs. For reflective optics, it turns out that the fixed-period designs are actually quite similar, so we do not lose a significant fraction of the efficiency in this compromise.

Finally, we calculate the mask functions $m_j(x, y)$ that define the lithographic etching steps, where the steps are labeled by the index j. This calculation combines the phase function $\Delta\phi(x, y)$ and the grating design function $H(d/\Lambda)$. The

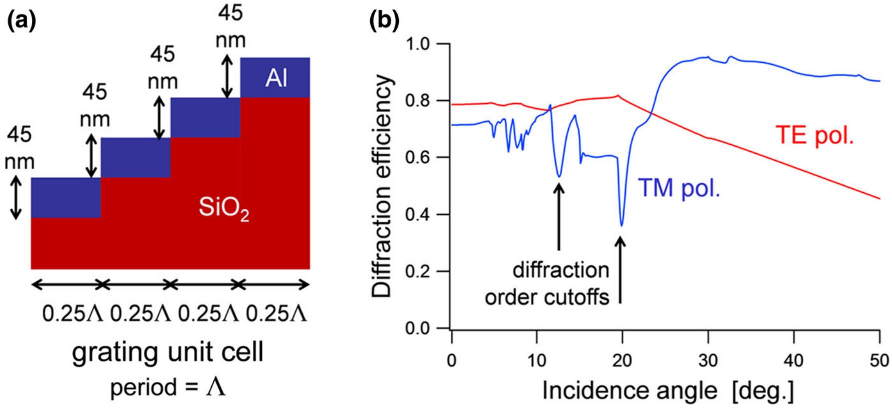

Fig. 2 A grating design for reflective diffractive optics fabricated on an ion trap. **a** Unit cell representation of grating. *Red*: silicon dioxide; *blue*: aluminum overcoating. **b** Diffraction efficiency simulation, indicating efficiency over 60 % for numerical aperture up to 0.7 (Color figure online)

design of Fig. 2 can be realized using only two etch steps: one with etch depth 90 nm, over regions $d/\Lambda \in [0, 1/2)$, and one with etch depth 45 nm, over regions $d/\Lambda \in [0, 1/4) \cup [3/4, 1)$. Since the phase function advances by 2π over a period Λ, the etch regions with $d/\Lambda \in [a, b]$ are the same as the regions with $\Delta\phi(x, y) \in 2\pi[a, b)$ for any $a, b \in [0, 1)$. For a four-level design, the mask functions are therefore given by

$$m_1(x, y) = \begin{cases} 1 & \Delta\phi(x, y) \in [0, \pi) \\ 0 & \text{otherwise} \end{cases} \tag{3}$$

$$m_2(x, y) = \begin{cases} 1 & \Delta\phi(x, y) \in [0, \pi/2) \cup [3\pi/2, 2\pi) \\ 0 & \text{otherwise} \end{cases} \tag{4}$$

where 1 denotes that the region is to be etched and we have wrapped the phase function $\Delta\phi(x, y)$ so that it only takes on values in the range $[0, 2\pi)$.

For high-numerical-aperture diffractive mirrors operating in the ultraviolet, the desired minimum feature size can be < 200 nm, and therefore these devices are most easily fabricated using electron beam lithography. In a standard direct-write process, a thin resist layer is spun onto the substrate and is exposed in the desired pattern using a focused electron beam. Removal of exposed resist and etching of the substrate forms the desired height patterning on the substrate. For multilevel designs, multiple lithography steps can be performed as discussed above, as long as the alignment between successive steps is much smaller than the minimum feature size [23,24]. Possible alternatives are the direct-write and grayscale lithography techniques, both of which use a single exposure step to define a near-continuous range of feature heights [25].

3 Planar waveguide circuits

In our architecture, light is collected from, and delivered to, the diffractive mirrors through planar waveguide circuits (PLCs) fabricated in lithium niobate (LN). These scalable, compact optical devices are based on arrays of monolithically fabricated waveguides that control, deliver, and collect light across the entire trap array. Reconfigurability is provided by the electro-optic effect: Switches and modulators with GHz bandwidth are integrated with the waveguide arrays and are used to manipulate light in the classical and quantum regime [26].

Robust, tight integration with the trap can be achieved by mounting the PLCs directly to the trap carrier inside the vacuum system while using a time multiplex scheme for the excitation and collection of light that reduces the infrastructure to a single input fiber and a single output fiber. Monolithic fabrication of GHz bandwidth electro-optic devices on the PLCs enables arbitrary optical excitation and collection sequences to be implemented at each site in the ion array on nanosecond timescales.

3.1 Fabrication and properties of planar waveguide circuits

The requirement of fast routing of photons to/from different sites and the need for high optical transmission in the UV make lithium niobate (LN) the ideal platform for this architecture. LN is one of the most common substrates for commercial integrated optical devices. Its transparency window ranges from 350 nm to 4.1 μm [27], making it an attractive candidate for working with such ions as Yb^+, Ca^+, and Ba^+. This substrate has one of the largest electro-optic coefficients of any material ($r_{33} = 31$ pm/V), a great advantage for low-voltage sub-nanosecond optical switching [26]. An alternative substrate, lithium tantalate (LT), presents a transparency window down to 280 nm, making it suitable for working with Be^+.

High-quality optical waveguides can be fabricated in LN through the standard techniques of reverse proton exchange (RPE) [28] and titanium indiffusion [29]. In RPE:LN waveguides, the index contrast between core and cladding is $\Delta n = 0.03$ at 370 nm, one order of magnitude larger than Ti:LN waveguides. Hence, RPE:LN waveguides support much smaller bending radius than Ti:LN waveguides and are preferred for complex PLCs.

In proton exchanged waveguides, the core is fabricated by replacing lithium ions (Li^+) with hydrogen ions (H^+) by dipping the sample in a benzoic acid bath. The effect on the substrate is to increase the extraordinary refractive index and decrease the ordinary one [27]. A subsequent annealing step in air is performed to reduce the H^+ concentration and improve the optical properties of the waveguide in terms of propagation losses and nonlinearity. The third step of RPE buries the waveguide under the crystal surface and increases the circular symmetry of the optical mode. This last step is extremely important in order to increase the coupling with optical fiber and to reduce the surface scattering losses.

RPE waveguides only guide light polarized along the optic axis. As discussed below, this is a significant but not fatal restriction for QIP implementations. By choosing the crystal cut of each PLC wafer, we are also free to choose the polarization direction relative to the PLC plane. A Z-cut wafer will guide light polarized orthogonal to the plane of the substrate, while an X-cut wafer will guide a mode with in-plane polarization. The mode parameters for the different wafer cuts can be made identical with

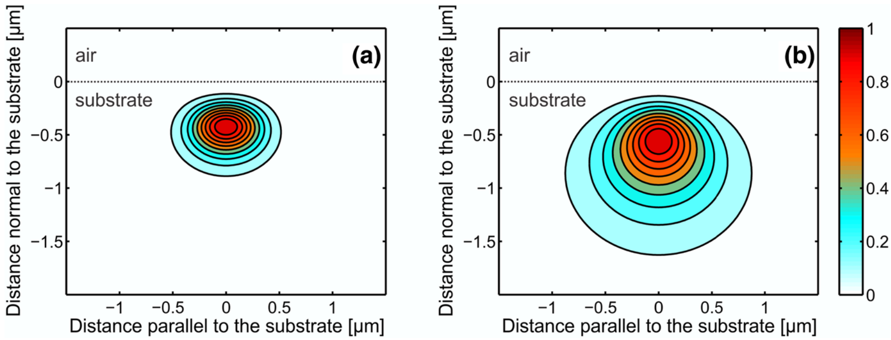

Fig. 3 Waveguide modes in lithium niobate. The colormap shows the mode intensity normalized to the peak intensity. Simulations are carried out for 370 nm. **a** A mode optimized for small bending radius and tolerance to fabrication error. **b** A larger mode with lower numerical aperture, suitable for input/output coupling

appropriate control over the fabrication process [30]. The polarization can therefore be chosen independently for each of the four PLC layers in our architecture.

Although LN-PLCs are most commonly used in the IR and visible, they appear promising for UV applications as well. The main differences are that the near-UV wavelengths used for Yb^+ and Ca^+ lie near the edge of the transparency window of LN, and UV wavelengths are more susceptible to scattering loss due to waveguide imperfections. We have simulated the fabrication of RPE waveguides that support single-mode guiding at 370 nm. By combining the fabrication process parameters with diffusion models and the material properties of LN, we are able to obtain an accurate model of the refractive index profile and the waveguide mode [30]. The left panel of Fig. 3 shows a mode obtained for channel width of 1 μm, initial proton exchange depth of 0.3 μm, annealing time of 15 min at 328 °C, and RPE time of 15 min at 328 °C. This mode is optimized for resistance to bending loss and fabrication error, making it suitable for fabrication of devices on the PLC. However, its numerical aperture is approximately 0.35, which would make integration between the PLC and the ion trap difficult (see Sect. 3.2). By reducing the channel width to 0.5 μm, we can obtain a spatially larger mode with numerical aperture below 0.2. Adiabatically tapering to the larger mode enables straightforward integration with the trap as well as high coupling efficiency to single-mode fiber.

The loss in a PLC is directly related to the complexity of the circuit architecture. For the bending-tolerant waveguide mode of Fig. 3, we estimate that a single 1×2 electro-optic switch occupies 0.5 cm of waveguide path length. We have performed a preliminary characterization of RPE-LN waveguides at the Yb^+ principal transition wavelength of 370 nm. The propagation losses were found to be below 0.9 dB/cm. A typical PLC might incorporate a cascade of 6 MZIs, enough to temporally multiplex excitation and fluorescence for $\sim$16 ions with independent switching and frequency control. Such a PLC will have a loss of $\lesssim$3 dB. In the near-UV wavelengths of interest here, the power handling capability of a single waveguide is approximately 2 mW [31].

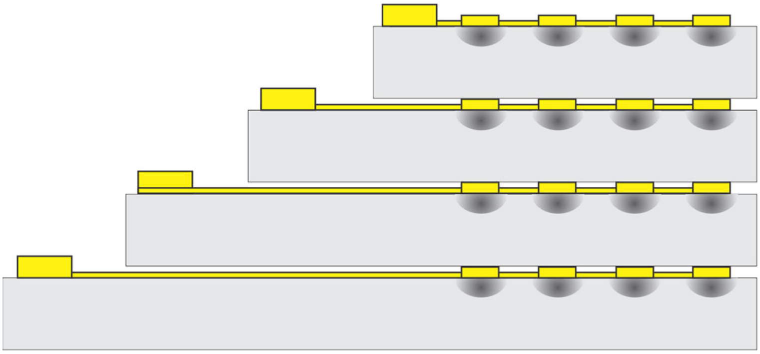

Fig. 4 Multilayer stacking of PLCs for full electrode access. The view direction is in the plane of the PLC substrates. *Gold*: electrodes. *Gray*: waveguide modes

While a single PLC can only address a single row of mirrors, it is also useful to consider multiple rows of mirrors addressed by multilayer PLCs as in Fig. 1. To construct such a multilayer PLC, each PLC layer can be fabricated independently and the layers can be bonded using either O_2 plasma activation [32] or gold-bump bonding [33]. In order to match the distance between arrays of diffractive elements, the waveguide substrate can be thinned down by lapping to the desired thickness before bonding. For several of the PLC layers, the electro-optic devices end up being sandwiched between substrates, but it is still necessary to provide independent electrical connections to each device. To this end, one can use substrates of different lateral sizes for the different layers, leaving electrical bonding pads exposed for each layer, as shown in Fig. 4.

3.2 Matching PLCs to diffractive mirrors

We aim to design diffractive mirrors that convert efficiently between the desired spatial mode at the trap array site and the fixed spatial mode of the waveguide, without the use of additional optical elements. As we show, this task is feasible for both efficient fluorescence collection and delivery of excitation light into a tight focus. We analyze the problem for an ideal mirror with unit diffraction efficiency in order to clearly convey the results; the diffraction efficiency depends considerably on the quality and sophistication of the fabrication process, and is therefore best treated separately. The spatial mode associated with the array site may be the mode of a focused laser beam (in the case of excitation) or an atomic dipole mode (in the case of fluorescence collection). In trapped-ion QIP, ion fluorescence is always a more scarce resource than laser power. Hence, most of the available solid angle on the chip surface will be reserved for fluorescence collection, and excitation modes will be restricted to relatively low numerical aperture.

The analysis is most easily carried out in the plane of the trap chip. The geometry is shown in Fig. 5. We define the coordinate system in the chip plane such that $\hat{x}$ lies along the local RF nodal line of the trap (the "RF rail"), $\hat{y}$ lies in the plane of the trap surface, but transverse to the RF nodal line, and $\hat{z}$ is the normal to the trap surface. Both

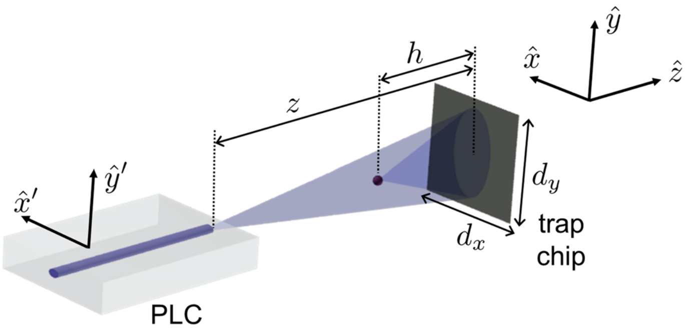

Fig. 5 Schematic of waveguide/chip mode-matching geometry

the mirror and the end facet of the PLC are normal to $\hat{z}$ and are separated by a distance z_0. As discussed above, the PLC waveguide mode is not cylindrically symmetric, so we also specify the waveguide axes $\hat{x}'$ and $\hat{y}'$ in the plane of the end facet, with $\hat{y}'$ being the normal to the substrate.

First we consider the waveguide mode: As it turns out, this mode can be well modeled by an elliptical Gaussian beam. For the mode of Fig. 3, which is most relevant here, the mode overlap with the best-fit elliptical Gaussian is $\eta_{\text{wg-}G} = 0.93$ with $1/e^2$ waist radii of 0.68 μm along $\hat{x}'$ and 0.54 μm along $\hat{y}'$. The waveguide mode at the mirror can be written as

$$\mathbf{E}_{\text{wg}} = \boldsymbol{\epsilon}_{\text{wg}} E_{0,\text{wg}}(x, y) \exp[i\phi_{\text{wg}}(x, y)] \tag{5}$$

where $\boldsymbol{\epsilon}_{\text{wg}}$ is the polarization vector of the waveguide mode and $E_{0,\text{wg}}(x, y)$, $\phi_{\text{wg}}(x, y)$ are the magnitude and phase of the electric field. Note that $E_{0,\text{wg}}$ is taken to be real. Since the waveguide modes considered here have numerical apertures $\sim$0.2, we are justified in taking the polarization vector to be independent of spatial position.

Since excitation modes have low numerical aperture, it is easy to design an appropriate mirror and estimate the mode coupling efficiency. The excitation mode $\mathbf{E}_{\text{exc}}$ can be written in the same form as Eq. (5) and can also be taken to approximate an elliptical Gaussian beam. The spatial phase function of the mirror should be set equal to $\Delta\phi(x, y) = \phi_{\text{exc}}(x, y) - \phi_{\text{wg}}(x, y)$, where the phases ϕ_{wg}, ϕ_{exc} are given by the standard Gaussian beam propagation formulas [34]. The mode coupling efficiency is then computed as

$$\eta_{\text{wg-exc}} = \eta_{\text{wg-G}} \left|\boldsymbol{\epsilon}^*_{\text{wg}} \cdot \boldsymbol{\epsilon}_{\text{exc}}\right|^2 \frac{\left|\int p_{\text{mir}} E_{0,\text{wg}} E_{0,\text{exc}}\, \mathrm{d}x\mathrm{d}y\right|^2}{\int |E_{0,\text{wg}}|^2\, \mathrm{d}x\mathrm{d}y \int |E_{0,\text{exc}}|^2\, \mathrm{d}x\mathrm{d}y} \tag{6}$$

where $p_{\text{mir}}(x, y)$ is equal to 1 inside the mirror area and 0 outside. In practice, we first choose a waveguide mode and mirror geometry. Then we calculate the best Gaussian approximation to the excitation mode by maximizing Eq. (6) with respect to the waist sizes of $E_{0,\text{exc}}$ at the mirror. Finally, we calculate the mirror spatial phase function required for coupling. In this paper, we consider rectangular mirrors with axes that lie along the principal axes of the elliptical waveguide mode. In this case, analytic calculations suffice to find the approximate excitation mode. Specific examples will be discussed in Sects. 4.1 and 4.2 below.

The analysis of fluorescence collection is more challenging. At the high numerical apertures considered here, the atomic dipole radiation pattern received at the mirror is quite different to that for a spherical wave and the electric field polarization varies considerably across the mirror surface. At each point on the mirror, the dipole field can be broken up into a TE-polarized field, which lies in the plane of the mirror, and a TM-polarized field, which has a significant component normal to the mirror surface. The TE field simply experiences a phase shift given by the mirror spatial phase $\Delta\phi(x, y)$. However, since the mirror is designed to convert the high-NA dipole wave into a TEM wave propagating normal to the mirror, the TM field experiences a rotation into the mirror plane as well as a phase shift. Since we are considering an ideal mirror, the magnitude of the TM field remains unchanged, but the new TM field is orthogonal to the TE field and to $\hat{z}$. We write the dipole field just after reflection as

$$\mathbf{E}_{\text{dip}} = \boldsymbol{\epsilon}_{\text{dip}}(x, y) E_{0,\text{dip}}(x, y) \exp[i\phi_{\text{dip}}(x, y)] \tag{7}$$

Here $\phi_{\text{dip}}(x, y) = 2\pi i r/\lambda$, where r is the distance from the ion to the point (x, y) on the mirror. In general, the field polarization vector $\boldsymbol{\epsilon}_{\text{dip}}(x, y)$ is spatially varying (although after reflection, it lies in the $\hat{x}$-$\hat{y}$ plane).

Fortunately, in the cases of interest, the dipole field after reflection can be quite well approximated by an elliptical Gaussian with a spatially uniform field polarization, even at extremely high-NA. The electric field of this "collected" mode, $\mathbf{E}_{\text{coll}}$, can be written in the same form as Eq. (5). The dipole field depends on the orientation of the quantization axis $\mathbf{B}$ and the atomic transition polarization (π, σ^+, or σ^-). In the "equatorial" view, with $\mathbf{B}$ lying in the $\hat{x}$-$\hat{y}$ plane, both π and $\sigma^\pm$ fluorescence are well described in terms of a collected mode. In the "polar" view, $\mathbf{B} \parallel \hat{z}$, only $\sigma^\pm$ fluorescence can be modeled; in [35] it was shown that the overlap with a Gaussian vanishes for polar π fluorescence. For the equatorial π and $\sigma^\pm$ cases and for the polar $\sigma^\pm$ case, we compute the overlap factor

$$\eta_{\text{dip-coll}} = \frac{\left| \int (\boldsymbol{\epsilon}^*_{\text{dip}}(x, y) \cdot \boldsymbol{\epsilon}_{\text{coll}}) p_{\text{mir}} E_{0,\text{wg}} E_{0,\text{exc}} \, \mathrm{d}x\mathrm{d}y \right|^2}{\int |E_{0,\text{dip}}|^2 \, \mathrm{d}x\mathrm{d}y \int |E_{0,\text{coll}}|^2 \, \mathrm{d}x\mathrm{d}y} \tag{8}$$

between the dipole mode and the collected mode, and maximize $\eta_{\text{dip-coll}}$ with respect to the elliptical Gaussian waist parameters of the collected mode. For NA ≤ 0.93, the equatorial π and polar $\sigma^\pm$ configurations can achieve $\eta_{\text{dip-coll}} \geq 0.85$. For equatorial $\sigma^\pm$, the approximation is rather worse, with $\eta_{\text{dip-coll}} \geq 0.55$.

We can now calculate the mirror design and the single-mode collection efficiency for fluorescence collection. The mirror spatial phase function is given by $\Delta\phi(x, y) = \phi_{\text{wg}}(x, y) - \phi_{\text{coll}}(x, y)$. We define the single-mode collection efficiency into the waveguide, η_{coll}, as the fraction of power emitted on the atomic transition that is collected into the waveguide mode.

$$\eta_{\text{coll}} = \eta_{\text{wg-G}} C_{\text{mir}} \eta_{\text{dip-coll}} \eta_{\text{coup}} \tag{9}$$

$$\eta_{\text{coup}} = \left| \boldsymbol{\epsilon}^*_{\text{wg}} \cdot \boldsymbol{\epsilon}_{\text{coll}} \right|^2 \frac{\left| \int p_{\text{mir}} E_{0,\text{wg}} E_{0,\text{coll}} \, \mathrm{d}x \mathrm{d}y \right|^2}{\int |E_{0,\text{wg}}|^2 \, \mathrm{d}x \mathrm{d}y \int |E_{0,\text{coll}}|^2 \, \mathrm{d}x \mathrm{d}y} \tag{10}$$

Here C_{mir} is the fraction of the dipole intensity that strikes the mirror area (as computed in, e.g., [7]). The mode coupling between the collected mode and the Gaussian approximation to the waveguide mode is given by η_{coup}.

The fluorescence collection efficiency is determined by the collection mirror geometry: As discussed above, fluorescence collection will usually have first priority in determining the allocation of surface area to the various mirrors. Our rectangular mirrors have widths D_x, D_y along $\hat{x}$, $\hat{y}$. The ion height h is fixed by the electrode structure of the trap, so that only the normalized widths $d_{x,y} = D_{x,y}/h$ are actually relevant, and we have $C_{\text{mir}} = C_{\text{mir}}(d_x, d_y)$ and $\eta_{\text{dip-coll}} = \eta_{\text{dip-coll}}(d_x, d_y)$. The waveguide mode shape fixes $\eta_{\text{wg-G}}$ and the Gaussian beam parameters controlling $E_{0,\text{wg}}$. For a given mirror geometry, the waveguide-chip distance z controls the spot size of the Gaussian-approximated waveguide mode at the mirror. Hence we optimize η_{coup} with respect to z, obtaining $\eta_{\text{coup,opt}}(D_x/h, D_y/h)$ and thus the optimized collection efficiency

$$\eta^{\text{opt}}_{\text{coll}}(d_x, d_y) = \eta_{\text{wg-G}} C_{\text{mir}}(d_x, d_y) \eta_{\text{dip-coll}}(d_x, d_y) \eta_{\text{coup}}(d_x, d_y) \tag{11}$$

for a given mirror geometry. We may also wish to explicitly include the mirror area as a resource when attempting to optimize the density of array sites. To this end we define an additional figure of merit

$$F_{\text{coll}} = \frac{\eta^{\text{opt}}_{\text{coll}}(d_x, d_y)}{d_x d_y} \tag{12}$$

Results of these calculations for a particularly useful waveguide/ion configuration are shown in Fig. 6. In this configuration, termed "$\pi \;\|$," the quantization axis lies along the RF nodal line $\hat{x}$ and the crystal cut of the waveguide substrate is chosen so that π-polarized light is guided. Collection is therefore in the equatorial view. The waveguide substrate lies in the $\hat{x}$-$\hat{z}$ plane (i.e., $\hat{x}' \parallel \hat{x}$), so that each array site lying along the RF node can be matched to a waveguide. In this case, the major axis of the waveguide mode is orthogonal to that of the dipole mode, so that the collection efficiency is optimum when the mirror is square.

For a mirror with unit diffraction efficiency, Fig. 6a shows that the single-mode collection efficiency can reach $\sim$30 % for NA $\sim$0.97, i.e., allowing incidence angles up to 70°. It remains to be seen whether realistic grating designs can maintain high diffraction efficiency over such a high-NA. On the other hand, from Fig. 6b, we see that the area-weighted figure of merit F_{coll} is optimized for $d_x \approx d_y \lesssim 2.5$, i.e., for incidence angles up to $\sim$50°. Over this range, the grating design of Fig. 2 retains diffraction efficiency over 50 %. Owing to fundamental constraints of the electric field configuration in planar microfabricated traps, it is unlikely that the spacing of independently controllable trap array sites can be less than 2.5h in any event. Virtually

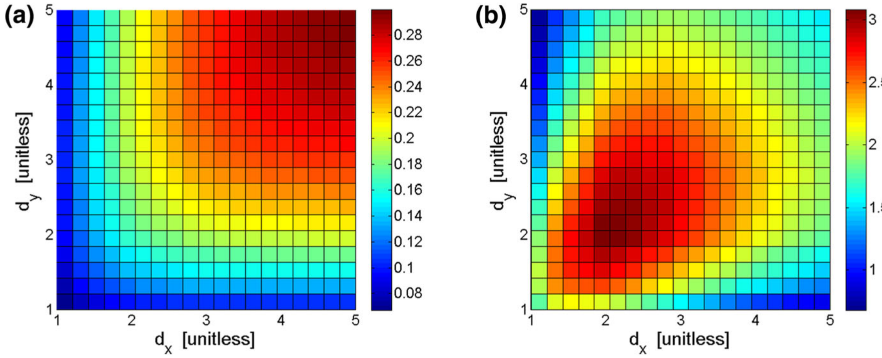

Fig. 6 Fluorescence collection efficiency for $\pi \parallel$ configuration. **a** Single-mode collection efficiency as a function of normalized mirror widths. **b** Figure of merit for area-weighted collection according to Eq. (12)

any scenario in our architecture therefore features a realistic fluorescence collection efficiency over 10 %, including the effects of finite diffraction efficiency.

Although the waveguide-chip distance z is fixed by mode-matching requirements, it turns out that the proximity of the waveguide to the chip does not pose significant problems. At the area-optimized collection NA of $\sim$0.7, probably the lowest NA of interest for applications, we calculate the waveguide-chip distance to be $z \sim 4h$, so that the waveguide is placed $3h$ above the ion position. At higher NA, z increases further. For a typical surface trap, the RF potential is negligible this far above the surface, while any distortions of the DC fields are small and readily compensated. In addition to the distortion of trapping fields, it is well known that bare dielectric surfaces placed near a trap are also prone to static charge buildup. The resulting electric fields would be significant for a bare waveguide facet at this position [36]. Coating the waveguide facet with a thin layer of indium tin oxide, a conductive material that is transparent in the near-UV, can alleviate the static charging [13]. One could also consider coating the facet with metal, but in this case some masking is necessary so that the metal does not cover the waveguides themselves. Note that this straightforward integration scenario requires the use of a low-NA waveguide mode like that shown in Fig. 3b. For the smaller, more bending-tolerant mode of Fig. 3a, we find $z \sim 2h$ at NA ~ 0.7 and the interference with the RF potential is likely to be significant. In practice, one can use the bending-tolerant mode for the internal waveguide circuitry of the PLC, with adiabatic tapering to the lower-NA mode at the PLC input and output.

We have performed similar fluorescence collection calculations for several other configurations, denoted $\pi\ \perp$, $\sigma\ \parallel$, $\sigma\ \perp$, and σ-pol. Here the atomic transition is either π or $\sigma^{\pm}$, while $\perp$ or $\parallel$ indicates an equatorial view ($\mathbf{B} \perp \hat{z}$) with waveguide substrate $\hat{x}'$ either normal ($\perp$) or parallel ($\parallel$) to $\mathbf{B}$. The σ-pol configuration uses a polar view ($\mathbf{B} \parallel \hat{z}$); owing to the cylindrical symmetry of the radiation pattern in this view, the waveguide substrate orientation is irrelevant. The orientation of the elliptical waveguide mode turns out to affect the collection efficiency only by a few percent, even for NA > 0.97. Instead, the major differences between configurations arise from the different radiation patterns for the atomic polarizations. The collection efficiencies for equatorial π and polar $\sigma^{\pm}$ are roughly equal, while the equatorial $\sigma^{\pm}$ efficiency is half as large. The optimum mirror geometries and waveguide-mirror distances are roughly the same for all three cases. Hence, the $\pi \parallel$, $\pi \perp$, and σ-pol configurations will be of most interest for applications.

3.3 Arrays of single-photon detectors

Scalable state readout of trapped ions requires arrays of photodetectors with high quantum efficiency at the detection wavelength. A highly scalable, mature detector technology already exists, in the form of arrays of silicon single-photon avalanche diodes (SPADs) [37]. The overall performance of these innovative devices is extremely good in terms of detection efficiency (50 % at 480 nm), dark count rate ($\sim$7 kHz), and timing jitter ($\sim$100 ps). Using a standard CMOS process, the Yb^+ wavelength of 369 nm, the SPAD efficiency is about 15 %, about a factor of 2 below the best currently available photomultiplier tubes. However, single SPAD detectors are commercially available with 40 % quantum efficiency at 350 nm, indicating that similar quantum efficiency could be obtained for SPAD arrays by optimizing the fabrication process.

Such SPAD detectors are fabricated using standard CMOS process and they can be realized in linear (1D) and square (2D) arrays with hundreds of units. Because SPADs fabrication is compatible with standard microelectronic processing, time-tagging and counting logic can in principle be integrated on the same substrate of the detectors allowing fast read-out of multiple qubits simultaneously [38,39]. The detector–waveguide interface can be realized by bonding the SPAD array to the PLC facet with UHV-compatible epoxy.

4 Implementation of QIP operations

Our architecture enables full optical integration of trapped-ion quantum computation, including all the basic operations of the KMW architecture as well as photonically mediated remote ion–ion entanglement. A possible realization for a linear array of N sites is shown in Fig. 7. Each array site is addressed by four diffractive mirrors. The first mirror performs collection of fluorescence. The second provides illumination with resonance radiation for laser cooling, qubit state readout, or ion–photon entanglement generation. Finally, two more mirrors excite the ions with off-resonant light from different directions, enabling the implementation of Raman logic gates. The total array of $4 \times N$ mirrors is divided into four groups of N according to function. Each functional array is served by a separate PLC, making a stack of four PLC layers in all. Each of these PLC layers is configured with N waveguides at the trap end to serve the N mirrors in its functional array. The $\pi \parallel$ configuration is highly suitable for QIP with $^{171}Yb^+$ and we primarily consider this configuration below. Unless otherwise noted, the mirror geometry is taken to be square with width $2.5h$, thus optimizing the area-weighted figure of merit for fluorescence collection, and the PLC-chip distance is optimized for fluorescence collection. The calculations of Sect. 3.2 then show that the $1/e^2$ radii of each waveguide mode are approximately $(W_x, W_y) = (0.71, 0.88)h$ at the chip surface. These design parameters, and others to be discussed below, are

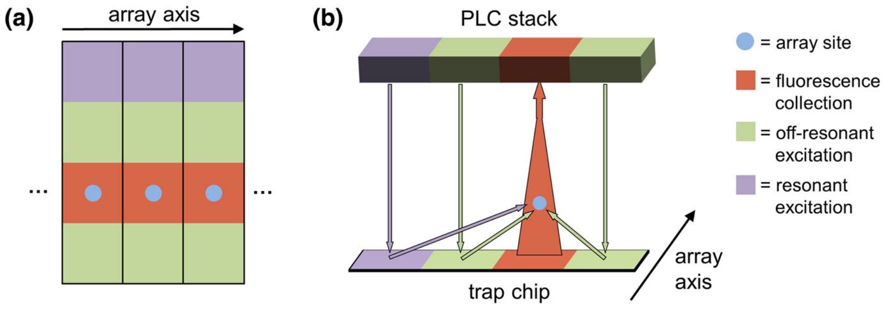

Fig. 7 Mirror/PLC configuration for general quantum computation. **a** Mirror configuration on trap chip. Each unit cell of the array (*black rectangle*) provides optical operations to the trap array site (*blue dot*) using four diffractive mirrors. **b** Side view of a single unit cell, illustrating coupling between the PLC stack and the mirror configuration (Color figure online)

collected in Table 1. The expected operating parameters for QIP in our architecture are summarized in Table 2 and will be justified in the following sections.

Electro-optic switches are integrated in each PLC layer so that all N waveguides in a PLC layer can be accessed via a smaller number of external input/output fibers [41]. Fluorescence from multiple sites is routed into a single waveguide using a cascade of electro-optically controlled Mach–Zehnder interferometers (MZIs). Conversely, excitation light from a single laser source can be routed to any array site; for instance, as illustrated in Fig. 7, 2^N sites can be routed toward a single output using N cascaded reconfigurable splitters. While using MZIs formed by two directional couplers is the standard solution, more compact devices can be fabricated using Y-junction splitters [42] or multimode-interferometric structures [43]. With careful design, the length of one MZI can be made as short as $\approx$5mm. Our measurements of waveguide loss (Sect. 3.1) then indicate $\zeta_{\mathrm{MZI}} \gtrsim 0.9$.

Multi-GHz frequency shifting of excitation light can be provided independently for each array site by integrated electro-optic modulators on the PLC. Integrated single-sideband optical modulation is readily achieved by combining phase modulators in a stable interferometric network [41,44]. Bandwidths up to 40 GHz have been demonstrated [45], sufficient to span the hyperfine intervals of any ion currently used for QIP. Each array site can be equipped with its own modulator. Hence, the complex frequency-shifting arrangements used for current trapped-ion experiments can be moved entirely onto the PLC. The time required to change frequencies can be $<$100 ps [45], much shorter than the $\sim$10 ns switching time of acousto-optic frequency shifters and much shorter than the atomic decay time. Hence, the operation speed is only limited by atomic properties.

4.1 State initialization and measurement

Both state initialization and state measurement of ion qubits are carried out by excitation with resonant light. State initialization proceeds by optical pumping, while measurement requires the detection of fluorescence. The intensity of the resonant light

Table 1 Summary of design parameters for our architecture

Parameter	Symbol	Typical value
Atomic parameters		
Resonant transition wavelength	λ	369.5 nm (Yb^+)
Off-resonant laser detuning	Δ	0.5–50 THz
Atomic lifetime	τ_{at}	8 ns (Yb^+)
Atomic saturation intensity	I_{sat}	50 mW cm^{-2} (Yb^+)
Geometric parameters		
Ion height above chip	h	50–200 μm
PLC-chip distance	z_{opt}	4 h
Mirror size	(d_x, d_y)	$(2.5, 2.5)h$
Mode parameters $(1/e^2$ *intensity radii*)		
Waveguide mode at PLC	$(w_{x',wg}, w_{y',wg})$	$(1.9, 1.5)\lambda$
Waveguide mode at chip	(W_x, W_y)	$(0.71, 0.88)h$
Resonant beam at array site	$(w_{x,res}, w_{z,res})$	$(3.6, 20)\lambda$
Off-resonant beam at array site	$(w_{x,res}, w_{z,res})$	$(2.2, 5.6)\lambda$
Optical processing parameters		
Fluorescence collection efficiency into PLC	η_{coll}	$\gtrsim 0.1$ ($\pi \parallel, \pi \perp, \sigma^{\pm}$polar)
		$\gtrsim 0.05$ ($\sigma^{\pm} \parallel, \sigma^{\pm} \perp$)
Transmission through one MZI on PLC	ζ_{MZI}	$\gtrsim 0.9$
Switching time		100 ps
Frequency modulation bandwidth		up to 40 GHz
Detector efficiency	P_{det}	0.15 (current SPAD array)
		0.4 (future SPAD arrays)
		0.3 (PMT)

is set at or above the atomic saturation intensity I_{sat} so that the operation time is minimized. At the same time, undesired resonant scattering from other ions (”crosstalk”) can and must be minimized to preserve qubit coherence. As will be seen, PLC switching is far faster than the operation time for state initialization or state measurement, so our architecture permits these operations to take place independently and asynchronously at each array site.

Saturation of the atomic transition can be reached with laser power of $\lesssim$10 nW per array site. In the design of Fig. 7, the diffractive mirror that directs resonant light to the ion has its center at a distance $y_{res} = 5h$ from the trap rail, so that the diffraction angle along $\hat{y}$ ranges from $\sim$75°–81°. The optimization of the grating design for such a mirror is outside the scope of the present work, but we note that the diffraction angle is nearly constant, a case that has been well studied by diffraction grating manufacturers. The waveguide mode striking the mirror is only somewhat elliptical, but the highly oblique reflection causes extreme ellipticity in the focused excitation mode. Hence, the

Table 2 Summary of QIP operating parameters for our architecture

Parameter	Symbol	Typical value
Initialization and measurement		
Laser power per array site		$\sim$10 nW
State preparation time	τ_{prep}	$\sim$300 ns
# photon counts for measurement	N_γ	10 (ref. [40])
# sites multiplexed for measurement	M_{meas}	3 – 10
Measurement time	τ_{meas}	$\sim$1 μs (π ∥, current SPAD array)
Crosstalk to adjacent array site		$\lesssim 2 \times 10^{-5}$
Crosstalk to adjacent ion in crystal		$\lesssim 2 \times 10^{-3}$
Phononic gates		
Laser power per array site	$\sim$100 μW	
Two-qubit gate time	$\sim$30 μs	
Crosstalk to adjacent ion in crystal	$\lesssim 1 \times 10^{-3}$	
Photonic interconnects		
# sites multiplexed for detection	M_γ	15
Transmission through multiplexing PLC		0.66
Entanglement rate per fiber		1750 s^{-1}

All laser powers are measured at the array site

excitation beam will propagate nearly parallel to the chip surface; the focused waist will be narrow along $\hat{x}$ and wide along $\hat{z}$. Since the mirror size is larger than the $1/e^2$ diameter of the waveguide mode, we can make a rough estimate of the spot size at the array site using standard Gaussian beam propagation formulas for a mirror of infinite aperture:

$$w_{x,\mathrm{res}} = \frac{2\lambda y_{\mathrm{res}}}{\pi W_x} \approx 1.7\,\mu\mathrm{m} \qquad w_{z,\mathrm{res}} = \frac{2\lambda y_{\mathrm{res}}^2}{\pi h W_y} \approx 6.7\,\mu\mathrm{m} \tag{13}$$

Initialization in the $^{171}\mathrm{Yb}^+$ $|F, m_F\rangle = |0, 0\rangle$ state can be performed using π-polarized light tuned to the $^2\mathrm{S}_{1/2}\,|F = 1\rangle - {}^2\mathrm{P}_{1/2}\,|F = 0\rangle$ transition near 369.5 nm [46,47]. In the π ∥ geometry, the excitation light is therefore required to be polarized along $\hat{x}$ as it exits the waveguide. A lower bound for the state initialization time is

$$\tau_{\mathrm{prep}} = 2\tau_{\mathrm{at}} \frac{\ln \epsilon_{\mathrm{prep}}}{\ln(1-\kappa)} \tag{14}$$

where the allowable initialization error is ϵ_{prep} and the branching ratio into the desired state is κ. For typical atomic lifetimes and branching ratios, and initialization error probability $\lesssim 10^{-3}$, one finds $\tau_{\mathrm{prep}} \sim 300$ ns. This timescale remains much larger than the 100 ps switching time for either intensity control or frequency shifting in PLCs.

Owing to the efficient collection of fluorescence in our architecture, the time required for a state measurement is on the order of 1 μs, much shorter than the

$10 - 30\,\mu\text{s}$ assumed in recent proposals for large-scale trapped-ion QIP [3,5,48]. For the variable definitions and typical numerical values given in Table 1, the state measurement time is equal to

$$\tau_{\text{meas}} = 2\tau_{\text{at}} \frac{N_\gamma}{\eta_{\text{coll}} \zeta P_{\text{det}}} \tag{15}$$

τ_{at} is the atomic lifetime, $N_\gamma \sim 10$ is the number of photons that must be detected to make a state measurement with error probability below 10^{-3} [40], η_{coll} is the fraction of fluorescence collected into the PLC, ζ is the transmission efficiency of the PLC and other optical components in the detection path, and P_{det} is the quantum efficiency of the detector. For large numbers of array sites, the PLC is likely to be the primary source of optical loss in the detection path. If M_{meas} sites are time-multiplexed onto a single path, then $\zeta \approx \zeta_{\text{MZI}}^M$. Optimal use of each detector at the PLC I/O end requires that M_{meas} is approximately equal to the fraction of time employed for detection at one site. Simulations of compiled error correction circuits indicate that ∼10–30 % of the operating time in a large trapped-ion quantum computer will be required for error syndrome measurement [49], implying $M_{\text{meas}} \sim 3 - 10$ and $\zeta > 0.5$. We therefore find the measurement time $\tau_{\text{meas}} \sim 1\,\mu\text{s}$.

The tight focusing afforded by diffractive mirrors enables ion-by-ion state initialization and readout within a single array site with minimal crosstalk to adjacent array sites. It may even be possible to initialize the state of one ion in a crystal while inducing only a slight decoherence on the neighboring ions. Note that w_x, the $1/e^2$ focused waist size along the trap rail, is much smaller than the typical ion–ion spacing of $\sim 10\,\mu\text{m}$ within a single array site. However, the off-axis intensity is higher than the naive Gaussian prediction owing to diffraction from the finite mirror aperture. For the parameters above, we find that the intensity drops to $< 2 \times 10^{-3}$ its maximum value at an off-axis distance of $\Delta x = \pm 10\,\mu\text{m}$ along the trap rail, and to $< 2 \times 10^{-5}$ its maximum value at the smallest possible array spacing of $\Delta x = \pm 125\,\mu\text{m}$. In the $\hat{z}$ direction, diffraction causes a small fraction of the total resonant power, $\sim 6 \times 10^{-3}$, to strike the trap surface. Scattering from the trap is primarily specular, so the $\hat{x}$ intensity sidelobes are likely to be the dominant source of undesired resonant scattering between array sites and between individual ions within an array site. Resonant scattering cross-talk between array sites is therefore limited to a level compatible with large-scale QIP.

4.2 Phononic quantum logic

To perform multiqubit gates between ions in a single array site, one applies laser fields that are *not* resonant with an allowed atomic transition [1]. These fields coherently couple the spin and motion of the ions, enabling transfer of quantum information through the shared phonon modes of the ion crystal. For $^{171}\text{Yb}^+$, a particularly favorable implementation uses two-photon stimulated Raman transitions to couple the $|F, m_F\rangle = |0, 0\rangle$ and $|1, 0\rangle$ states [50]. The two Raman laser beams counterpropagate, with both beams being normal to the trap axis, creating an optical force normal to $\hat{x}$.

The Raman laser frequency is detuned from the 369.5 nm resonance by at least 0.5 THz, so that intensities $\gtrsim 1\ \mathrm{kW\,cm^{-2}}$ are needed to achieve gate speeds on the order of $\sim 30\ \mu\mathrm{s}$ with 4 % gate error [50].

In our architecture, two Raman laser beams are allotted to each array site, and the two beams originate from different PLC/mirror layers spaced symmetrically about the RF rail (Fig. 7). Raman selection rules forbid driving two-photon π-π transitions in $^{171}\mathrm{Yb}^+$, so the Raman waveguide modes are polarized along $\hat{y}$. The diffractive mirrors have their centers placed at $y_{\mathrm{Raman}} = \pm 2.5h$ from the RF rail, so the Raman beams are reflected at quite oblique angles (50°–70°), similarly to the resonant beams. The polarization at the focus is therefore mostly along $\hat{z}$, but with a significant $\hat{y}$ component. Both σ^+ and σ^- atomic polarizations can be driven, allowing for two-photon $|F, m_F\rangle = |0, 0\rangle$ and $|1, 0\rangle$ transitions.

Addressing of single ions within an ion crystal, as required by the original Cirac–Zoller proposal for multiqubit gates [51], is straightforward in our architecture. Again using the approximation of Eq. (13), we find the $1/e^2$ focal radii to be $w_x \approx 0.83\ \mu\mathrm{m}$, $w_z \approx 2.1\ \mu\mathrm{m}$. In a Cirac–Zoller gate, the focused spot must strike different ions in the crystal at different points in the gate sequence; in our architecture, the focused laser spot is fixed and the trapping potential shifts the crystal back and forth to bring different ions into the focus. Crosstalk between array sites is again dominated by the $\hat{x}$ sidelobes of the focused beam, with the intensity (and thus the spin–spin coupling) dropping to $< 1 \times 10^{-3}$ its maximum value at the neighboring ion. Previous demonstrations of multiqubit gates based on single-ion addressing achieved good fidelity with far higher crosstalk, up to 5 % [52].

Many currently used gate protocols require the Raman laser intensity to be the same for every ion in a crystal [1]. Normally, this condition is fulfilled by using weakly focused Raman beams with waists that are larger than the total crystal size, so that high Raman power is needed to achieve the required intensities. However, the position of each ion within the crystal is easily calculated if the trap frequencies are known. It is then straightforward to design diffractive mirrors that focus the Raman beams in a multiple-spot pattern, such that each spot is centered on the position of each ion and every spot has equal intensity. Back-propagating the desired multiple-spot pattern to the diffractive mirror yields a phase and amplitude pattern that can be mode-matched to the input waveguide mode. Calculation of the required phase function has been discussed in Sect. 3.2, while amplitude modulation can be achieved by writing the grating pattern only on selected portions of the mirror area. The resolution limits of the multiple-spot pattern are again given by Eq. (13). Hence, a two-ion crystal with $10\ \mu\mathrm{m}$ ion–ion spacing can be addressed by two spots with $(w_x, w_y) = (0.83, 2.1)\ \mu\mathrm{m}$ rather than a single spot of waist radius $\gtrsim 10\ \mu\mathrm{m}$, representing an order-of-magnitude savings in laser power.

The optical power levels for the Raman beams remain compatible with switching and modulation through PLCs. Since the diffractive mirrors create a tight focus, a relatively modest power of $\sim 100\ \mu\mathrm{W}$, as measured at the array site, is sufficient to drive Raman gates. Hence, the few-mW power handling capability of PLCs (Sect. 3.1) is sufficient for tens of array sites to be driven simultaneously from a single fiber input. Switching of the two-photon detuning is again readily achieved through PLC frequency shifting.

4.3 Photonic quantum interconnects

Current schemes for large-scale trapped-ion quantum computing involve the use of short-range, photonically mediated quantum interconnects to supplement phononic ion–ion gates [3,53]. Probabilistic ion–photon entanglement at each end of the interconnect, followed by a Bell measurement on the two photons, creates entanglement between the ions at each end [54]. This entanglement can then be used as a computational resource, permitting communication of quantum information across the quantum computer without the need for ion shuttling or short-range phononic gates. Current experiments [55] achieve remote ion–ion entanglement rates on the order of 5 s^{-1} over a single optical channel. Proposals for large-scale interconnects envisage hundreds of array sites, each coupled to a single fiber. The photons are routed to Bell measurements through a large optical cross-connect switch (OCX) based on MEMS mirrors [3,6]. Such OCXs exhibit $\sim$10 µs switching time and insertion loss of only 2 dB for a 256×256 switch array operating in the infrared [56] (one expects higher loss in the UV, but data have not yet been published to our knowledge).

Our architecture offers efficient single-mode collection that can improve the data rate of such photonic quantum interconnects by nearly two orders of magnitude. The remote ion–ion entanglement probability scales as the square of the collection efficiency [54]. Despite the use of a high-NA objective in a recent experiment, the single-mode collection efficiency remained approximately 1.4 % [55]. The calculations of Sect. 3.2 show that realistic collection efficiencies exceed 10 % in our architecture, implying a $50\times$ increase in ion–ion entanglement rate. While RPE waveguides do not support polarization encoding of the photonic qubit, protocols for time-bin encoding are straightforward [35] and are favored for long-distance transmission. However, Ti:LN waveguides, discussed in Sect. 3.1, do support polarization encoding.

PLCs also offer high-speed time-domain multiplexing of the array sites, enabling a further order-of-magnitude improvement in interconnect data rate. The switching time for a MEMS-based OCX is much longer than the $\tau_{at} \sim 10$ ns time window for entangled photon emission. The rate-limiting step for ion–photon entanglement generation is the time required for re-initialization by optical pumping. Using PLCs, we can probe each site in turn for emission of an entangled photon while performing initialization on the other sites. Such a strategy maximizes the overall data rate and minimizes the number of fibers in the interconnect. Hence we should temporally multiplex $M_\gamma \sim \tau_{prep}/(2\tau_{at}) \gtrsim 15$ sites onto a single output mode for best use of resources. (Note that, for a time-bin entanglement protocol, we must allow for two emission time windows per trial.) The PLC transmission to the output mode is given by $\zeta_{MZI}^{\log_2 M_\gamma} \sim 0.66$, so PLC loss reduces the overall ion–ion entanglement rate to $0.4\times$ its nominal value. Nevertheless, the overall ion–ion entanglement rate across a single fiber is increased by a factor of 7. Note that both the SPAD detectors discussed in Sect. 3.3 and standard photomultiplier tubes are capable of time-tagging the detection events to within 1 ns, so it is straightforward to correlate detection events with their parent ions.

5 Conclusion

We have presented a tightly integrated, scalable optical architecture for trapped-ion QIP. On-chip diffractive mirrors have been shown to couple light efficiently between trap array sites and planar lightwave circuits. Both diffractive mirrors and PLCs are readily scalable to large numbers of array sites and can be microfabricated by standard techniques. All the fundamental QIP operations—state initialization, quantum logic, and state measurement—can be carried out entirely within our optical architecture. Photonic interconnects, a key requirement for the latest trapped-ion QIP schemes, are also easily implemented in our architecture.

All operational parameters are at least as favorable for our architecture as for current experiments, and in some regards, our architecture is distinctly superior. State measurement time is an order of magnitude faster and the laser energy required for each operation is an order of magnitude lower. The switching and frequency-shifting capabilities of PLCs enable much of the optical bench to be directly integrated on the PLC, improving the robustness and scalability of the laser system. Temporal multiplexing of optical excitation through PLCs enables optimal use of the total laser power: Lasers are switched between array sites without ever needing to be switched off. Temporal multiplexing of fluorescence collection reduces other resource requirements: The number of detectors needed for state detection and the number of trap-to-trap fibers needed for an optical interconnect are both reduced by an order of magnitude.

Our architecture may represent a significant advance toward field-deployable trapped-ion QIP devices, e.g., as quantum repeaters. Among the subsystems of a trapped-ion QIP device, the optical bench is uniquely delicate and comprises a large fraction of the total volume. With the optical integration afforded by our architecture, the optical bench can shrink to hold only the laser sources themselves—for many current experiments, laser frequency stabilization can be accomplished purely with high-quality optical wavemeters. With the advent of compact UV laser sources, it is easy to imagine that future trapped-ion QIP devices will require a free-space optical bench that is only tens of centimeters on a side. Such a bench would be the same size as the vacuum system, connected to it purely by optical fiber, with no possibility of optical misalignment. Using the architecture proposed here, we envision robust and portable trapped-ion QIP devices with form factor and power consumption similar to the recently commercialized portable Bose–Einstein condensate systems.

Acknowledgements This work was supported by the Australian Research Council (ARC) under DP130101613. D.K. was supported by ARC Future Fellowship FT110100513. E.W.S was supported by ARC Future Fellowship FT130100472.

References

1. Blatt, R., Wineland, D.: Entangled states of trapped atomic ions. Nature **453**, 1008–1015 (2008)
2. Kielpinski, D., Monroe, C., Wineland, D.J.: Architecture for a large-scale ion-trap quantum computer. Nature **417**, 709–711 (2002)
3. Monroe, C., Raussendorf, R., Ruthven, A., Brown, K., Maunz, P., Duan, L.M., Kim, J.: Large-scale modular quantum-computer architecture with atomic memory and photonic interconnects. Phys. Rev. A **89**(2), 022317 (2014)

4. Duan, L.M., Monroe, C.: Colloquium: quantum networks with trapped ions. Rev. Mod. Phys. **82**(2), 1209–1224 (2010)
5. Steane, A.M.: How to build a 300 bit, 1 giga-operation quantum computer. Quantum Inf. Comput. **7**, 171–183 (2007)
6. Kim, J., Kim, C.: Integrated optical approach to trapped ion quantum computation. Quantum Inf. Comput. **9**(3), 181–202 (2009)
7. Streed, E.W., Norton, B.G., Chapman, J.J., Kielpinski, D.: Scalable, efficient ion–photon coupling with phase Fresnel lenses for large-scale quantum computing. Quantum Inf. Comput. **9**, 0203–0214 (2009)
8. VanDevender, A.P., Colombe, Y., Amini, J., Leibfried, D., Wineland, D.J.: Efficient fiber optic detection of trapped ion fluorescence. Phys. Rev. Lett. **105**(2), 023001 (2010). doi:10.1103/PhysRevLett.105.023001
9. Streed, E.W., Norton, B.G., Jechow, A., Weinhold, T.J., Kielpinski, D.: Imaging of trapped ions with a microfabricated optic for quantum information processing. Phys. Rev. Lett. **106**(1), 010502 (2011). doi:10.1103/PhysRevLett.106.010502
10. Kim, T.H., Herskind, P.F., Chuang, I.L.: Surface-electrode ion trap with integrated light source. Appl. Phys. Lett. **98**(21), 214103 (2011)
11. Brady, G., Ellis, A., Moehring, D., Stick, D., Highstrete, C., Fortier, K., Blain, M., Haltli, R., Cruz-Cabrera, A., Briggs, R., Wendt, J., Carter, T., Samora, S., Kemme, S.: Integration of fluorescence collection optics with a microfabricated surface electrode ion trap. Appl. Phys. B: Lasers Opt. (2011). doi:10.1007/s00340-011-4453-z
12. Merrill, J.T., Volin, C., Landgren, D., Amini, J.M., Wright, K., Doret, S.C., Pai, C., Hayden, H., Killian, T., Faircloth, D., et al.: Demonstration of integrated microscale optics in surface-electrode ion traps. New J. Phys. **13**(10), 103005 (2011)
13. Eltony, A.M., Wang, S.X., Akselrod, G.M., Herskind, P.F., Chuang, I.L.: Transparent ion trap with integrated photodetector. Appl. Phys. Lett. **102**(5), 054106 (2013)
14. Jechow, A., Streed, E.W., Norton, B.G., Petrasiunas, M.J., Kielpinski, D.: Wavelength-scale imaging of trapped ions using a phase Fresnel lens. Opt. Lett. **36**, 1371–1373 (2011)
15. Kim, C., Knoernschild, C., Liu, B., Kim, J.: Design and characterization of MEMS micromirrors for ion-trap quantum computation. IEEE J. Sel. Top. Quantum Electron. **13**, 322–329 (2007)
16. Knoernschild, C., Kim, C., Liu, B., Lu, F.P., Kim, J.: MEMS-based optical beam steering system for quantum information processing in two-dimensional atomic systems. Opt. Lett. **33**, 273–275 (2008)
17. Crain, S., Mount, E., Baek, S., Kim, J.: Individual addressing of trapped ^{171}Yb+ ion qubits using a microelectromechanical systems-based beam steering system. Appl. Phys. Lett. **105**(18), 181115 (2014)
18. Gil, D., Menon, R., Smith, H.I.: The promise of diffractive optics in maskless lithography. Microelectron. Eng. **73–74**, 35 (2004)
19. Cruz-Cabrera, A., Kemme, S., Wendt, J., Kielpinski, D., Streed, E., Carter, T., Samora, S.: High efficiency DOEs at large diffraction angles for quantum information and computing architectures. In: Integrated Optoelectronic Devices 2007, pp. 648–650. International Society for Optics and Photonics (2007)
20. Shiono, T., Kitagawa, M., Setsune, K., Mitsuyu, T.: Reflection micro-Fresnel lenses and their use in an integrated focus sensor. Appl. Opt. **28**(16), 3434–3442 (1989)
21. Born, M., Wolf, E.: Principles of Optics, 7th edn. Cambridge University Press, Cambridge (1999)
22. Moharam, M.G., Grann, E.B., Pommet, D.A., Gaylord, T.K.: Formulation for stable and efficient implementation of the rigorous coupled-wave analysis of binary gratings. J. Opt. Soc. Am. A **12**(5), 1068–1076 (1995)
23. Ferstl, M., Kuhlow, B., Pawlowski, E.: Effect of fabrication errors on multilevel Fresnel zone lenses. Opt. Eng. **33**(4), 1229–1235 (1994)
24. Orihara, Y., Klaus, W., Fujino, M., Kodate, K.: Optimization and application of hybrid-level binary zone plates. Appl. Opt. **40**(32), 5877–5885 (2001)
25. O'Shea, D.C., Suleski, T.J., Kathman, A.D., Prather, D.W.: Diffractive Optics: Design, Fabrication, and Test. SPIE Press, Bellingham (2004)
26. Bonneau, D., Lobino, M., Jiang, P., Natarajan, C.M., Tanner, M.G., Hadfield, R.H., Dorenbos, S.N., Zwiller, V., Thompson, M.G., O'Brien, J.L.: Fast path and polarization manipulation of telecom wavelength single photons in lithium niobate waveguide devices. Phys. Rev. Lett. **108**, 053601 (2012). doi:10.1103/PhysRevLett.108.053601

27. Korkishko, Y.N., Fedorov, V.A.: Ion Exchange in Single Crystals for Integrated Optics and Optoelectronics. Cambridge International Science Publishing, Cambridge (1999)
28. Korkishko, Y.N., Fedorov, V.A., Morozova, T.M., Caccavale, F., Gonella, F., Segato, F.: Reverse proton exchange for buried waveguides in $LiNbO_3$. J. Opt. Soc. Am. A **15**(7), 1838 (1998). doi:10.1364/JOSAA.15.001838. http://josaa.osa.org/abstract.cfm?URI=josaa-15-7-1838
29. Schmidt, R.V., Kaminow, I.P.: Metal-diffused optical waveguides in $LiNbO_3$. Appl. Phys. Lett. **25**(8), 458–460 (1974). doi:10.1063/1.1655547. http://scitation.aip.org/content/aip/journal/apl/25/8/10.1063/1.1655547
30. Lenzini, F., Kasture, S., Haylock, B., Lobino, M.: Anisotropic model for the fabrication of annealed and reverse proton exchanged waveguides in congruent lithium niobate. Opt. Express **23**(2), 1748–1756 (2014)
31. Kintaka, K., Fujimura, M., Suhara, T., Nishihara, H.: Efficient ultraviolet light generation by $LiNbO_3$ waveguide first-order quasi-phase-matched second-harmonic generation devices. Electron. Lett. **32**(24), 2237–2238 (1996)
32. Tulli, D., Janner, D., Pruneri, V.: Room temperature direct bonding of $LiNbO_3$ crystal layers and its application to high-voltage optical sensing. J. Micromech. Microeng. **21**(8), 085025 (2011)
33. Takigawa, R., Higurashi, E., Suga, T., Kawanishi, T.: Air-gap structure between integrated $LiNbO_3$ optical modulators and micromachined Si substrates. Opt. Express **19**(17), 15739–15749 (2011)
34. Yariv, A.: Quantum Electronics, 3rd edn. Wiley, New York (1987)
35. Luo, L., Hayes, D., Manning, T., Matsukevich, D., Maunz, P., Olmschenk, S., Sterk, J., Monroe, C.: Protocols and techniques for a scalable atom-photon quantum network. Fortschritte der Physik **57**(11–12), 1133–1152 (2009)
36. Harlander, M., Brownnutt, M., Hänsel, W., Blatt, R.: Trapped-ion probing of light-induced charging effects on dielectrics. New J. Phys. **12**(9), 093035 (2010). http://stacks.iop.org/1367-2630/12/i=9/a=093035
37. Fishburn, M., Maruyama, Y., Charbon, E.: Reduction of fixed-position noise in position-sensitive single-photon avalanche diodes. IEEE Trans. Electron. Dev. **58**(8), 2354–2361 (2011). doi:10.1109/TED.2011.2148117
38. Tisa, S., Guerrieri, F., Tosi, A., Zappa, F.: 100 kframe/s 8 bit monolithic single-photon imagers. In: 38th European Solid-State Device Research Conference, 2008 (ESSDERC 2008), pp. 274–277. IEEE (2008)
39. Guerrieri, F., Tisa, S., Tosi, A., Zappa, F.: Two-dimensional SPAD imaging camera for photon counting. IEEE Photonics J. **2**(5), 759–774 (2010). doi:10.1109/JPHOT.2010.2066554
40. Hume, D.B., Rosenband, T., Wineland, D.J.: High-fidelity adaptive qubit detection through repetitive quantum nondemolition measurements. Phys. Rev. Lett. **99**, 120502 (2007)
41. Wooten, E.L., Kissa, K.M., Yi-Yan, A., Murphy, E.J., Lafaw, D.A., Hallemeier, P.F., Maack, D., Attanasio, D.V., Fritz, D.J., McBrien, G.J., et al.: A review of lithium niobate modulators for fiber-optic communications systems. IEEE J. Sel. Top. Quantum. Electron. **6**(1), 69–82 (2000)
42. Xie, X., Saida, T., Huang, J., Fejer, M.M.: Shape optimization of asymmetric Y-junction for mode multiplexing in proton-exchange lithium niobate waveguides. Proc. SPIE **5728**, 360–366 (2005). doi:10.1117/12.593475
43. Cui, J., Chang, W., Feng, L., Cui, F., Sun, Y.: MMI power splitters based on the annealed proton exchange (APE) technology. Proc. SPIE **6837**, 68371A (2007). doi:10.1117/12.757383
44. Shimotsu, S., Oikawa, S., Saitou, T., Mitsugi, N., Kubodera, K., Kawanishi, T., Izutsu, M.: Single side-band modulation performance of a $LiNbO_3$ integrated modulator consisting of four-phase modulator waveguides. IEEE Photonics Tech. Lett. **13**(4), 364–366 (2001)
45. Kawanishi, T., Sakamoto, T., Miyazaki, T., Izutsu, M., Fujita, T., Mori, S., Higuma, K., Ichikawa, J.: High-speed optical DQPSK and FSK modulation using integrated Mach–Zehnder interferometers. Opt. Express **14**(10), 4469–4478 (2006)
46. Balzer, C., Braun, A., Hannemann, T., Paape, C., Ettler, M., Neuhauser, W., Wunderlich, C.: Electrodynamically trapped Yb^+ ions for quantum information processing. Phys. Rev. A **73**, 041407 (2006)
47. Olmschenk, S., Younge, K., Moehring, D., Matsukevich, D., Maunz, P., Monroe, C.: Manipulation and detection of a trapped Yb^+ hyperfine qubit. Phys. Rev. A **76**(5), 052314 (2007)
48. Kim, J., Pau, S., Ma, Z., McLellan, H., Gates, J., Kornblit, A., Slusher, R.E., Jopson, R.M., Kang, I., Dinu, M.: System design for large-scale ion trap quantum information processor. Quantum Inf. Comput. **5**(7), 515–537 (2005)

49. Balensiefer, S., Kregor-Stickles, L., Oskin, M.: An evaluation framework and instruction set architecture for ion-trap based quantum micro-architectures. In: ACM SIGARCH Computer Architecture News, vol. 33, pp. 186–196. IEEE Computer Society (2005)
50. Kim, K., Chang, M.S., Islam, R., Korenblit, S., Duan, L.M., Monroe, C.: Entanglement and tunable spin–spin couplings between trapped ions using multiple transverse modes. Phys. Rev. Lett. **103**(12), 120502 (2009)
51. Cirac, J.I., Zoller, P.: Quantum computations with cold trapped ions. Phys. Rev. Lett. **74**, 4091–4094 (1995)
52. Schmidt-Kaler, F., Häffner, H., Riebe, M., Gulde, S., Lancaster, G.P.T., Deuschle, T., Becher, C., Roos, C.F., Eschner, J., Blatt, R.: Realization of the Cirac–Zoller controlled-NOT quantum gate. Nature **422**, 408–411 (2003)
53. Metodi, T.S., Thaker, D.D., Cross, A.W., Chong, F.T., Chuang, I.L.: A quantum logic array microarchitecture: Scalable quantum data movement and computation. In: Proceedings of the 38th Annual IEEE/ACM International Symposium on Microarchitecture, 2005 (MICRO-38), p. 12. IEEE (2005)
54. Moehring, D.L., Madsen, M.J., Younge, K.C., Kohn, J.R.N., Maunz, P., Duan, L.M., Monroe, C., Blinov, B.B.: Quantum networking with photons and trapped atoms. J. Opt. Soc. Am. B **24**, 300–315 (2007)
55. Hucul, D., Inlek, I., Vittorini, G., Crocker, C., Debnath, S., Clark, S., Monroe, C.: Modular entanglement of atomic qubits using photons and phonons. Nat. Phys. **11**, 37–42 (2014)
56. Neilson, D.T., Frahm, R., Kolodner, P., Bolle, C., Ryf, R., Kim, J., Papazian, A., Nuzman, C., Gasparyan, A., Basavanhally, N., et al.: 256 $\times$ 256 port optical cross-connect subsystem. J. Lightwave Tech. **22**(6), 1499–1509 (2004)